Rivalry at the Interface: Ion Desolvation and Electrolyte Degradation in Model Ethylene Carbonate Complexes of Li$^+$, Na$^+$, and Mg^{2+} with PF$_6^-$ on the Li$_4$Ti$_5$O$_{12}$ (111) Surface

Hristo Rasheev, Radostina Stoyanova,* and Alia Tadjer*

ACCESS | Metrics & More | Article Recommendations | SI Supporting Information

ABSTRACT: Spinel lithium titanate, Li$_4$Ti$_5$O$_{12}$ (LTO), emerges as a "universal" electrode material for Li-ion batteries and hybrid Li/Na-, Li/Mg-, and Na/Mg-ion batteries functioning on the basis of intercalation. Given that LTO operates in a variety of electrolyte solutions, the main challenge is to understand the reactivity of the LTO surface toward single- and dual-cation electrolytes at the molecular level. This study first reports results on ion desolvation and electrolyte solvent/salt degradation on an LTO surface by means of periodic DFT calculations. The desolvation stages are modeled by the adsorption of mono- and binuclear complexes of Li$^+$, Na$^+$, and Mg^{2+} with a limited number of ethylene carbonate (EC) solvent molecules on the oxygen-terminated LTO (111) surface, taking into account the presence of a PF$_6^-$ counterion. Alongside cation adsorption, several degradation reactions are discussed: surface-catalyzed dehydrogenation of EC molecules, simultaneous dehydrogenation and fluorination of EC, and Mg^{2+}-induced decay of PF$_6^-$ to PF$_5$ and F$^-$. Data analysis allows the rationalization of existing experimentally established phenomena such as gassing and fluoride deposition. Among the three investigated cations, Mg^{2+} is adsorbed most tightly and is predicted to form a thicker fluoride-containing film on the LTO surface. Gassing, characteristic for carbonate-based electrolytes with LTO electrodes, is foreseen to be suppressed in dual-cation batteries. The latter bears promise to outperform the single-ion ones in terms of durability and safety.
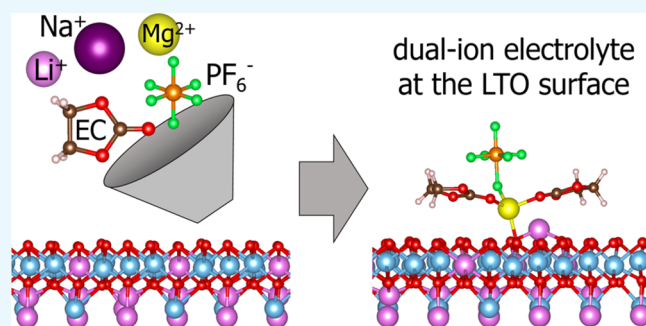
INTRODUCTION

The constantly growing renewable energy market demands cheaper, safer, and more efficient batteries for large-scale energy storage.[1,2] Among the different batteries, the Li-ion ones are indisputably the most versatile and widely used, particularly for portable devices.[3] Notwithstanding the undeniable advantages of these batteries, major shortcomings are their cost and exploitation safety. A practical and environmentally sustainable strategy to satisfying the global demands of Li-ion batteries while avoiding their drawbacks is the partial[4−6] or complete replacement of Li ions as charge carriers with ions of more abundant elements like Na, Mg, Ca, and Al.[7−10] In the case of total Li replacement, leading competitive alternatives of Li-ion batteries are Na- and Mg-ion batteries. The partial Li replacement produces the so-called hybrid metal-ion batteries (HMIBs), which, in principle, combine the advantages of Li-ion batteries (high energy density, well-established high-performance electrode materials and electrolytes, etc.) and those of Na or Mg ones (low cost, low toxicity, etc.).[5] Both single and hybrid metal-ion batteries function according to the same mechanism comprising the reversible intercalation of metal ions shuttling through electrolytes between the two electrodes,[1−5] which is why all

metal-ion batteries come across common issues. A major one is the choice of appropriate electrode material.[3] In this respect, lithium titanium spinel oxide Li$_4$Ti$_5$O$_{12}$ (LTO) represents a "universal" electrode for both single and hybrid metal-ion batteries since it is able to intercalate Li$^+$, Na$^+$, and Mg^{2+} ions.[11−15] The main advantages of LTO are negligible volume change during Li$^+$ cycling reactions (so called zero-strain insertion material),[16] high electrode potential (1.55 V vs Li^0/Li$^+$), avoidance of Li dendrite formation, nontoxicity, and thermal stability.[11]
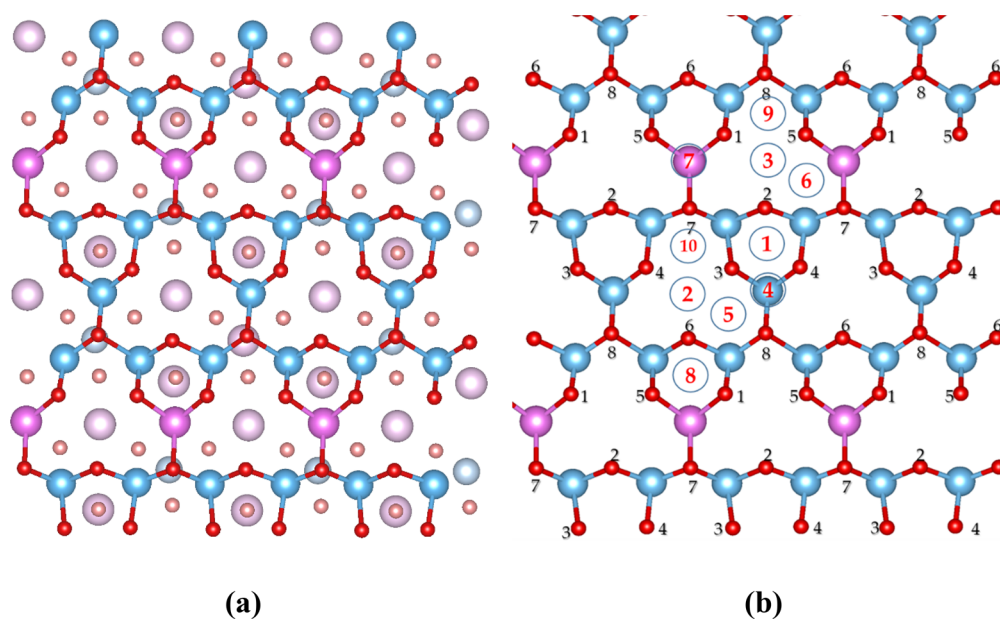
The next issue is closely related to the transport properties of electrolytes, which in turn depend on their solvation ability. The most commonly used class of solvents in Li-ion batteries, the organic carbonates (i.e., ethylene carbonate (EC), propylene carbonate (PC), dimethyl carbonate (DMC), etc.), are also suitable for Na-ion batteries but are unpropitious
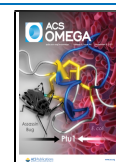
Figure 1. (a) Top view of the (111) face of $Li_4Ti_5O_{12}$. Color code: oxygen, red; lithium, pink; titanium, blue. Fading colors signify deeper positions. (b) Labeled oxygen types (black numbers) and adsorption sites (red numbers).

for Mg-ion batteries.[17] Successful and operational electrolyte compositions in hybrid Li-Mg and Na-Mg cells utilize short-chain polyethers like dimethoxyethane as solvent.[18,19] The impediment of organic carbonate usage in single or hybrid Mg-ion batteries is associated with solvent reduction instability on the surface of a Mg anode, which leads to the formation of a passivating layer.[20] This complication has been elegantly resolved by the deposition of Mg^{2+}-conducting polymeric film on the surface of the Mg anode, thus permitting the use of organic carbonates even in Mg-containing batteries.[21] In single-cation carbonate-based electrolytes, both experimental and theoretical studies demonstrate that Li^+ and Mg^{2+} are strongly solvated,[22,23] while the weakly solvated Na ions diffuse across electrolyte faster than Li^+ and Mg^{2+}.[24,25] In dual Li/Na EC-based electrolytes, earlier computational studies reveal that there is no competition between Li^+ and Na^+ and each ion is solvated as fully as solvent availability permits.[26] In contrast, in dual Li(Na)-Mg electrolytes at low and moderate degrees of solvation, the most stable species are heteronuclear complexes $Li^+Mg^{2+}(EC)_n$ and $Na^+Mg^{2+}(EC)_n$, which is why they determine electrolyte behavior at the surface.[27] Thus, the ionic transport property of the Mg-based electrolyte is improved significantly by addition of Li^+ or Na^+ ions, which has a direct impact on the rate capability of hybrid Li/Mg- and Na/Mg-ion batteries.[17,18,28]

Other concerns are closely related to the processes occurring at the electrode/electrolyte interface. Several competitive reactions take place near the electrode surface such as ion desolvation, ion adsorption, surface deposition of chemical products of the electrolyte decomposition (i.e., formation of SEI), and ion diffusion through SEI,[29] the interplay between which controls electrode performance.[30] A critical step preceding the intercalation of metal ions into the electrode is their desolvation.[31] On one hand, in order to fully dissolve the salt, the solvent has to solvate the ions very well; on the other hand, the interaction between the cation and the solvent (i.e., the solvation energy) has to be moderate, ensuring unobstructed desolvation prior to intercalation and, thus,

efficient working rates of the battery. In single-cation carbonate-based electrolytes, the energy barriers for desolvation of lithium and magnesium ion–solvent complexes are higher than that of sodium,[32,33] while in mixed-cation electrolytes, the formation of binuclear complexes leads to easier desolvation of the ions in comparison to mononuclear Li, Na, and Mg complexes. The desolvation is also sensitive toward the nature of the electrolyte counterion (e.g. PF_6^-, BF_4^-, $TFSI^-$, etc.).[34,35] In the case of incomplete solvation, the counterion complements the coordination shell around the metal ion, thus making the consecutive release of solvent molecules easier.[27] Most of these findings rely on molecular modeling, where, for simplicity, the effect of the electrode surface is not explicitly accounted for. Experimentally, it has been well documented that for the conventional graphitic electrode, the formation of SEI film has a direct impact on the desolvation process.[36,37] In comparison with graphitic electrodes, the surface layer on an LTO electrode is thinner since the electrochemical reaction takes place at a higher potential.[38] Ample research efforts have been devoted to the elucidation of desolvation in Li^+ electrolytes on graphite anodes,[39-41] while the desolvation processes in dual-cation electrolytes and their dependence on the electrode surface remain unclear from a fundamental point of view.

This study aims to gain insight into the desolvation process in single- and dual-cation electrolytes containing Li^+, Na^+, and Mg^{2+} with account of a model (111) surface of LTO. Ethylene carbonate is selected as solvent due to its polarity and high coordinating affinity toward Li^+, Na^+, and Mg^{2+}. The desolvation stages are modeled by the adsorption of mono- and binuclear complexes of Li^+, Na^+, and Mg^{2+} with a limited number of ethylene carbonate molecules on the oxygen-terminated LTO (111) surface. To rationalize the electrode surface effect on the desolvation process, the findings are compared with corresponding results obtained in vacuo and in implicit solvent. The counterion (PF_6^-) presence and its role in the desolvation process are also discussed. To the best of
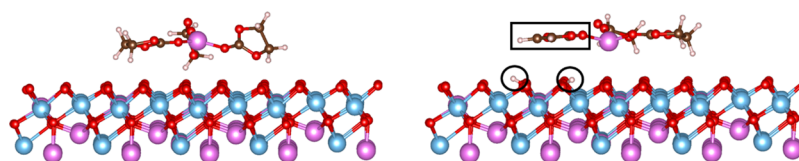
Figure 2. Initial (left) and optimized (right) geometry of Li$^+$(EC)$_3$ at ④. An aspect exhibiting the planarity of the vinylene carbonate (boxed) and the adsorbed hydrogens (encircled) is chosen.
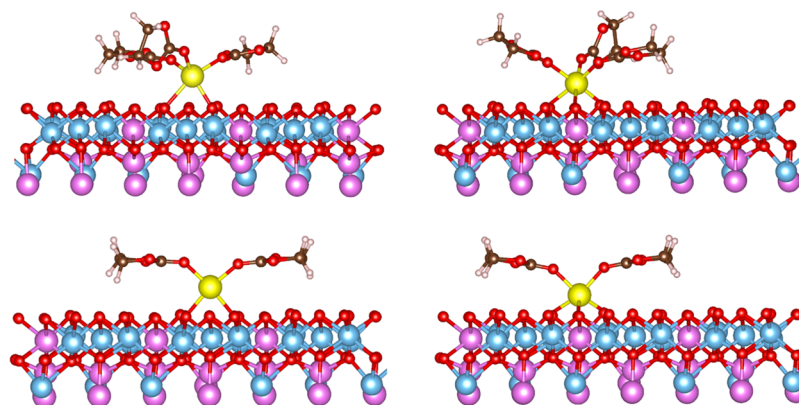
Figure 3. Optimized geometries of Mg^{2+}(EC)$_3$ placed at ④ (left) and at ③ (right).

RESULTS AND DISCUSSION

Adsorption Sites for Li$^+$, Na$^+$, Mg^{2+}, and EC on the (111) Surface. The model surface is the oxygen-terminated (111) LTO. The model is constructed to preserve the stoichiometry and the symmetry of the oxide bulk. The oxygens at the surface are nonidentical, since they differ both in height/depth and in the type of closest neighbors: 3Ti, 2Ti/1Li, 2Ti, and 1Ti/1Li (Figure 1). Thus, eight types of oxygen (black numbers) featuring different charges can be distinguished (Table S2).

The metal ions from the electrolyte are expected to adsorb at positions with copious oxygen proximity. The surface oxygens define 10 dissimilar adsorption sites as illustrated on Figure 1 (red numbers). The adsorption sites include positions on top of a metal node (i.e., sites ④ and ⑦) or in cavities formed by oxygen and metal atoms (the remaining sites). Inspection of the model (111) plane shows that each possible adsorption site is surrounded by three oxygens, defining triangles of different surface area as well as different oxygen types and summed charges. These data are collected in Table S3 (Supporting Information). To determine the most attractive adsorption site, we have placed a single metal ion at each position presented in Figure 1b and optimized the geometry of the system. The results obtained (Table S4) showed that ② and ③ are the most preferred sites for adsorption, while the least favorable position is ④ (Supporting Information).

In contrast to the metal cations, the solvent is insensitive to the dissimilar surface sites. Upon adsorption, however, the optimized geometry of a bare EC molecule results in dehydrogenation (Figure S2a). Planar vinylene carbonate (VC) is formed, while the abstracted hydrogens are bound to the surface. This EC instability is in line with the experimentally established gas generation upon LTO soaking in pure ethylene carbonate.[42]

Adsorption of Mononuclear M$^+$(EC)$_n$ Complexes and Their Desolvation. As a starting point, models of single ions with zero to three ECs placed on adsorption sites ③ and ④ of the rigid Li$_4$Ti$_5$O$_{12}$ surface are constructed (Figures 2 and 3). After geometry optimization, the data about the charges and averaged distances from the cation (Li$^+$, Na$^+$, and Mg^{2+}) to the EC carbonyl oxygens and to the oxygens from the spinel surface, as well as the energy difference between the two adsorption positions at different degrees of solvation are collected in Tables 1 and 2. All adsorbates placed at ③ retain

Table 1. Energy Difference $E④ - E③$ (in eV) between (EC)$_n$-Metal-Ion Clusters Placed Initially at Positions ④ and ③ Depending on the Degree of Solvation n

n	Li$^+$	Na$^+$	Mg^{2+}
0	0.40	0.49	2.15
1	0.20	0.30	[b]
2	0.19	0.28	0.83
3	[a]	0.07	0.06

[a]Placement at ④ results in EC degradation to VC + adsorbed 2H, while placement at ③ does not, so comparison is impossible. [b]Upon optimization, the cluster moves from ④ to ②.

their position, whereas some of those placed initially at ④ deviated toward either ① or ②. Nevertheless in all cases, the complexes adsorbed at ③ had lower energy than those positioned initially at ④ (Table 1). This demonstrates that the conclusions drawn for the preferred surface sites of the "naked" single ions hold for their EC complexes as well.

On the other hand, the energy difference $E④ - E③$ decreases with the increase of ECs, which indicates that the fully solvated ions are indifferent to the inhomogeneity of the surface and only become sensitive to the different adsorption sites after a certain degree of desolvation. Not only the number but also the orientation of the EC molecules matter: Models

Table 2. Values of AIM Charges (q) and Average Distances (in Å) from Cations to EC Carbonyl Oxygens (M^{p+}-O_{EC}) at Different Degrees of Solvation and to the Spinel Oxygens (M^{p+}-O_{sp}) upon Adsorption at Site ④ and ③ (Figure 1b)

	n	q_{Li^+}	Li^+-O_{EC}	Li^+-O_{sp}	q_{Na^+}	Na^+-O_{EC}	Na^+-O_{sp}	$q_{Mg^{2+}}$	Mg^{2+}-O_{EC}	Mg^{2+}-O_{sp}
④	0	0.98		1.96	0.93		2.41	1.73		2.10
	1	0.88	1.88	2.09	0.91	2.24	2.53	a	a	a
	2	0.90	1.89	2.37 (2)^b	0.91	2.26	2.63	1.75	1.97	2.09 (2)^b
	3	0.90	1.92	3.10 (2)^b	0.92	2.32	2.79	1.68	2.03	2.19 (2)^b
③	0	0.94		2.02	0.92		2.28	1.74		1.96
	1	0.89	1.92	2.14	0.91	2.29	2.41	1.73^a	1.99^a	2.04^a
	2	0.89	1.96	2.34	0.90	2.30	2.52	1.69	2.03	2.15
	3	0.93	1.90	3.49	0.91	2.35	2.69	1.76	2.06	2.30

^{a}Mg^{2+}EC converged to the same geometry irrespective of the initial placement. ^{b}Typically, the cation is coordinated by three oxygens from the spinel; the exceptions are given in parentheses.
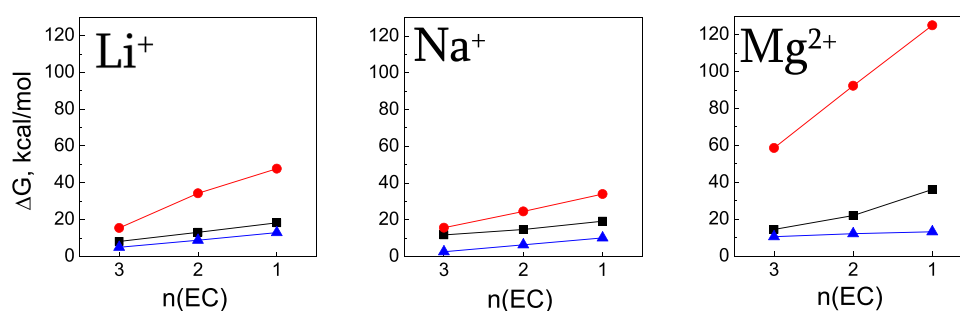
Figure 4. Free energy of desolvation in vacuo (red circles), in implicit solvent (blue triangles), and at the (111) face of Li$_4$Ti$_5$O$_{12}$ (black squares). Numerical data can be found in Table S5.

with the EC normal to the surface are less stable than those with ECs (roughly) parallel to the surface (Figure S2b). Obviously, the ECs also interact with the surface, although this van der Waals interaction is an order of magnitude weaker than the ionic-type coupling of the ion with the surface. However, this interaction is sensitive to the kind of metal ions (Li$^+$, Na$^+$, or Mg^{2+}) and their adsorption position, as well as to the number of EC molecules. Particularly in the case of Li$^+$ adsorbed at position ④, the optimization of Li$^+$(EC)$_3$ resulted in the abstraction of two hydrogen atoms from each of the CH$_2$ groups of an EC molecule and in conversion of the nonplanar ethylene carbonate into a planar VC, evolving an H$_2$ molecule (Figure 2). This did not occur in the (EC)$_n$ models of Na$^+$, Mg^{2+}, or Li$^+$ at site ③. Thus, the data disclose the complexity in the interaction of EC with the LTO (111) surface that could be related to experimental observations of gassing of LTO after storing in EC-based electrolytes.[43,44] It is thought that Ti centers on the LTO surface could act as a catalyst for solvent decomposition or oxygen atoms from the (111) plane could initiate the dehydrogenation and decarbonylation of alkyl carbonate solvents.[45,46] Gassing is a well-established phenomenon when LTO is used as an electrode in lithium-ion batteries, but it is underinvestigated in sodium- and magnesium-ion batteries. Our findings allow to predict that the availability of Li$^+$ ions in carbonate-based electrolytes will provoke more gassing reactions on LTO in comparison with Na$^+$ and Mg^{2+} ions.

Furthermore, a more general trend emerging from the geometry analysis (Table 2) is that both types of averaged distances between the cation and the closest oxygens— to the EC oxygens (M^{p+}-O_{EC}) and to the spinel surface oxygens (M^{p+}-O_{sp})—decrease upon desolvation; this makes the oxygen packing of the metal ion more compact and numerically closer to the respective lattice values of the corresponding oxides.

Another observation is that these distances are always larger for adsorption at ③ than for adsorption at ④. This is less pronounced for Na$^+$, more significant for Li$^+$, and most marked for Mg^{2+}. This seems to be in contradiction with the above discussed fact that site ③ is more favorable from an energetic point of view. However, an inspection of the geometries shows that while Na$^+$ always makes contact with three spinel oxygens irrespective of the adsorption site, the other two cations more often make two contacts when placed at ④ and three contacts when positioned at ②/③ (Figure 3). On the other hand, while the distance to the ECs depends only on the strength of the ion−solvent interaction, the distance to the spinel oxygens is restricted by the lattice parameters of the surface to values larger than 1.9 Å. Thus, the observation is in line with the difference in the surface areas presented in Table S3.

The charge transfer between ions and surroundings depends on the type of cation, too. The positive charge of the monovalent ions is highest in the absence of solvent and lowest in the presence of one EC irrespective of their position on the surface. In other words, charge transfer grows with desolvation, but when the solvent is removed completely, the electron density exchange with the surface is weaker, specifically at ④ and particularly for Li$^+$. The results for Mg^{2+} do not show any clear dependence neither on the number of ECs nor on the type of adsorption site. On the average, the charge loss is less than 10% for monovalent ions and above 15% for Mg^{2+}.

The desolvation energy of the three ions was calculated according to eq 1 and represented in Figure 4 and Table S5. The results are compared with earlier studies on the desolvation energy of the same ions in vacuo and in highly polar ($\varepsilon \sim 90$) implicit solvent.[27] As expected, the removal of the last solvent molecules is growingly endothermic in a relatively narrow range in polar medium. The presence of the surface compensates for the lost solvent molecules. The
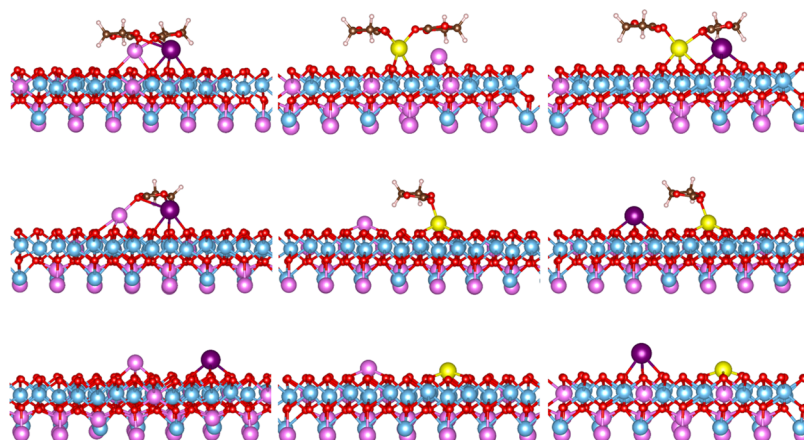
Figure 5. Optimized geometries of the last steps of desolvation of binuclear complexes: $Li^+Na^+(EC)_{2-0}$ (left), $Li^+Mg^{2+}(EC)_{2-0}$ (center), and $Na^+Mg^{2+}(EC)_{2-0}$ (right). Color code: Li^+, pink; Na^+, violet; Mg^{2+}, yellow.

Table 3. Values of AIM Charges (q), Distances between Cations, and Average Distances from Cations to EC Carbonyl Oxygens (M^{p+}-O_{EC}) and to the Spinel Ones (M^{p+}-O_{sp}) at Different Degrees of Solvation n upon Adsorption at the (111) Face of $Li_4Ti_5O_{12}$ [a]

$Li^+Na^+(EC)_n$						
n	$R(Li^+\text{-}Na^+)$	$R(Li^+\text{-}O_{EC})$	$R(Na^+\text{-}O_{EC})$	$R(Li^+\text{-}O_{sp})$	$R(Na^+\text{-}O_{sp})$	$q(Li^+)$	$q(Na^+)$
0	6.82			1.95	2.29	0.88	0.91
1	4.08	2.02	2.67	2.18	2.36	0.89	0.91
2	3.10	1.99	2.58	2.24	2.45	0.89	0.91
$Li^+Mg^{2+}(EC)_n$						
n	$R(Li^+\text{-}Mg^{2+})$	$R(Li^+\text{-}O_{EC})$	$R(Mg^{2+}\text{-}O_{EC})$	$R(Li^+\text{-}O_{sp})$	$R(Mg^{2+}\text{-}O_{sp})$	$q(Li^+)$	$q(Mg^{2+})$
0	6.99			1.96	1.96	0.97	1.75
1	5.86	5.60	2.00	1.99	2.04	0.91	1.75
2	3.90	4.76	1.99	1.99	2.05	0.88	1.76
$Na^+Mg^{2+}(EC)_n$						
n	$R(Na^+\text{-}Mg^{2+})$	$R(Na^+\text{-}O_{EC})$	$R(Mg^{2+}\text{-}O_{EC})$	$R(Na^+\text{-}O_{sp})$	$R(Mg^{2+}\text{-}O_{sp})$	$q(Na^+)$	$q(Mg^{2+})$
0	7.11			2.28	1.96	0.92	1.72 ②
1	5.90	5.39	2.06	2.28	2.04	0.88	1.73 ②
2	3.54	3.77	2.04	2.32	2.08	0.87 ②	1.75 ①

[a] All entries for distance are in Å.

difference in the desolvation behavior in polar and nonpolar environments depends on the charge density of the cation—the higher the charge density of the ions, the more prominent the medium influence. For the monovalent ions, the desolvation energy profile at the surface is strictly parallel to the one in solvent, shifted up by ~5 kcal/mol for Li^+ and by ~9 kcal/mol for Na^+, which signifies that the implicit solvent models give a trustworthy estimate of the surface phenomena.

The higher values at the surface are partly due to the simplicity of the model, including only the polarity of the electrode surface but ignoring the polarity of the electrolyte. However, the difference between the desolvation energy of free-standing clusters in vacuo and at the electrode surface can provide a rough estimate of the adsorption energy. Figure 4 and Table S6 reveal that the adsorption on the surface of Na^+ is the weakest while that of Mg^{2+} is the strongest, i.e., the higher the charge density of the adsorbing ions, the stronger the interaction with the surface. This is in good agreement with the charge loss variations upon desolvation (Table 2).

Adsorption of Binuclear $M_1^{p+}M_2^{q+}(EC)_n$ Complexes and Their Desolvation. In dual-ion electrolytes, earlier studies revealed that the scarcity of solvent favors the formation of hetero-binuclear complexes of the type $M_1^{p+}M_2^{q+}(EC)_n$.[27] Therefore, we have modeled all binuclear combinations of Li^+, Na^+, and Mg^{2+} with n = 0, 1, 2, 3 adsorbed on the studied surface (Figure 5 and Figure S3). Unlike the single-cation EC clusters, in this case, the adsorption cannot be equally favorable for both ions, so we tested different starting geometries. The averaged results for the structural characteristics are collected in Table 3 and Table S7.

All models feature identical trendlines in the variation of the monitored parameters: upon desolvation in the adsorbed clusters, the distance between the cations and from the cations to the solvent increases and the one to the surface decreases. However, the range of variation is markedly dissimilar. Since the $(EC)_3$ complexes have a completely different orientation versus the surface (Figure S3 and Table S7), these results are incomparable with the $(EC)_{0-2}$ ones and are therefore not presented in the main text.

In monovalent combinations, the ion−EC distance changes in a concurrent manner for the two cations, Li^+ keeping somewhat closer than Na^+. In heterovalent combinations, however, the monovalent ion is completely desolvated,

whereas Mg^{2+} behaves as in a single-ion model (Table 3). Regarding the average distance to the spinel oxygens, the cations exhibit identical conduct irrespective of the partner ion. The larger number of ECs shields the repulsion and keeps the cations at a distance within the range of 3−4 Å: The higher the charge density, the farther. Upon complete removal of the solvent, the cations diffuse to energetically favorable sites on the surface at ca. 7 Å apart.

The data for the charges is influenced by the fact that in the presence of solvent, typically only one of the cations adsorbs at preferred positions. However, it is obvious that the positive charge of the partner with lower charge density remains constant or slightly grows upon desolvation. Inversely, the charge of the partner with higher charge density decreases more sizably upon desolvation. These trendlines can be regarded as an indication that in binuclear clusters, alongside shielding, the solvent molecules mediate some charge exchange between the cations.

The desolvation penalty of the dual-cation clusters (Table 4) is lower than the sum of the desolvation energies of the single

Table 4. Energy Change (in kcal/mol) upon Desolvation of Dual-Ion/EC Clusters at the Spinel Surface[a]

| $n^{\#}$	Li^+Na^+	Li^+Mg^{2+}	Na^+Mg^{2+}
2	15.81	22.34	15.74
1	25.77	35.02	32.69

[a] $n^{\#}$ denotes the number of the removed EC molecule in the corresponding desolvation step.

cations with the same number of ECs (Table S5 and Figure 4), which can be interpreted as an indication that binuclear complexes are more prone to desolvation. Naturally, the combination Li^+Mg^{2+} requires the largest energy input, and Li^+Na^+ requires the smallest. This may be of significance in the search for electrolytes for Mg-ion batteries.

Furthermore, for adsorbed binuclear complexes, the data indicate that EC is not interacting chemically with the LTO surface unlike the case of adsorbed single Li^+-complexes. The weaker "electrode−solvent" interaction reflects the stronger involvement of EC in the complex with two ions rather than in that with one ion (Figures 2, 3, and 5), thus avoiding the gassing.

Counterion Effect on the Surface Behavior of Mono- and Binuclear Complexes. The above considerations referred solely to the desolvation conduct of cations, since they are the focal point of our interest. The next step is the inclusion of a counterion in the calculation scheme.

It is impossible to assess the desolvation energy of PF_6^- employing the same calculation protocol used for the cations because the process of anion desolvation is accompanied by side reactions, which makes the scheme inapplicable. The bare PF_6^- is repelled by the surface at about 5 Å (Figure 6, top). The complex PF_6^-EC undergoes an intricate transformation (Figure 6, middle), during which one EC hydrogen is adsorbed at the surface, its place taken by a fluorine. As a result, a fluorinated EC and a neutral PF_5 molecule are formed, the negative charge being spread on the surface. Bearing in mind that PF_5 is a highly reactive gas at room temperature, its formation is more than unwanted. However, this is repeated in the case of $PF_6^-(EC)_2$—one of the ECs is fluorinated, the other EC is dehydrogenated and converted into vinylene carbonate, three hydrogens are adsorbed at the surface (two of
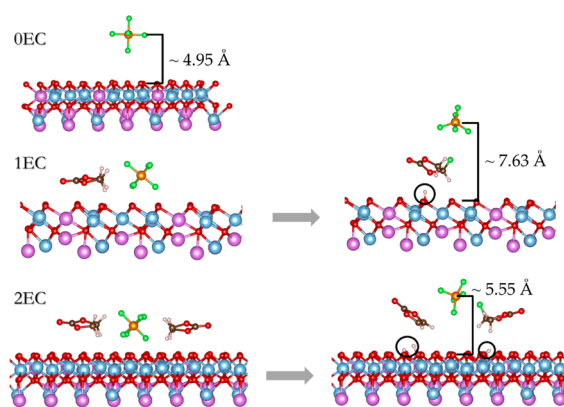
Figure 6. Optimized geometry of PF_6^- (top), initial and optimized geometry of PF_6^-EC (middle), and $PF_6^-(EC)_2$ (bottom) at the LTO surface.

them at a distance allowing the formation of H_2), and a neutral PF_5 is released (Figure 6, bottom).

We expected that the proximity of a cation would change the picture, so we modeled the ion pairs $Li^+PF_6^-(EC)_n$, $n = 0, 1$, and 2 (Figure 7). The optimized geometries revealed that the counterion plays the part of a solvent molecule as it does in the absence of an electrode surface.[27]

The bare $Li^+PF_6^-$ pair adsorbs in a predictable manner on the LTO surface, the anion complementing the coordination of Li^+. In $Li^+PF_6^-$ EC, the attraction of Li^+ holds the EC molecule close to the LTO surface, which results in the catalytic dehydrogenation of EC and formation of VC. $Li^+PF_6^-$ $(EC)_2$ displays the behavior of Li^+ $(EC)_3$ in which one solvent molecule is replaced by PF_6^-—even the distances Li^+-O_{EC} and Li^+-F_{PF6}^- are identical (Table 5)—and again, one of the ECs is converted into a VC. Similar destructive effects are observed for the respective complexes of Na^+ and Mg^{2+} (Table S8).

The data in Table 5 show that the ion−counterion distance is essentially constant irrespective of the EC number, but the distances from Li^+ to the LTO surface are larger than those in the absence of counterion (Table 2). With the increase of ECs, the counterion gets closer to the solvent and farther from the surface. While the charge of Li^+ remains constant, that of the counterion grows with the number of ECs. Although no desolvation energy can be quantified, the observations give evidence that the account of the counterion will not change the established trendlines; it would rather facilitate the cation desolvation, but this occurs at the expense of solvent destruction and formation of unwelcome by-products.

In the presence of a counterion, solvent destruction is not only a specificity of lithium complexes with EC. The same picture is observed when Li^+ is replaced by Na^+ (Figure 7 and Table S8). In $Na^+PF_6^-EC$, Na^+ is coordinated simultaneously by the counterion, the solvent molecule, and three oxygen atoms from the LTO surface. This pattern of complexation leads to the close proximity of EC to the LTO surface, which in turn makes favorable the release of at least 1 H from the solvent molecule.

In $Mg^{2+}PF_6^-EC$, the simultaneous interaction of Mg^{2+} with the LTO surface and counterion produces a decomposition of PF_6^- with the release of neutral PF_5 and a F^- anion, the latter being bonded to the adsorbed Mg^{2+} (Table S8 and Supporting Information). The addition of one EC does not prevent the decomposition of the counterion: Mg^{2+} is coordinated by three oxygens from LTO, the released from PF_6^- fluoride ion, and
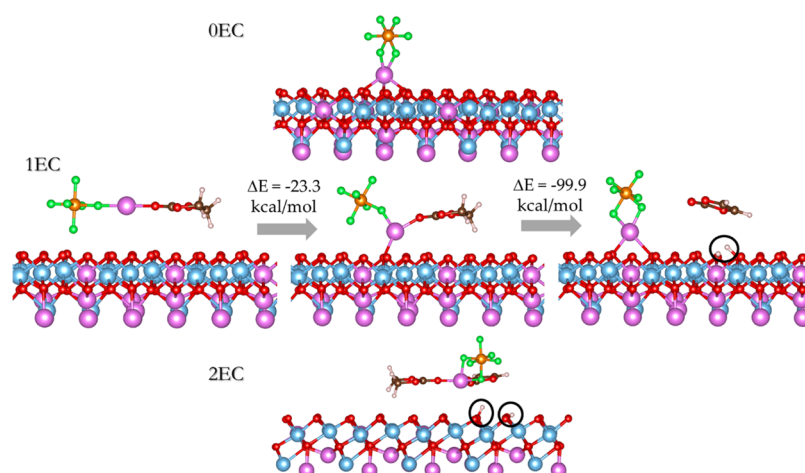
Figure 7. Optimized geometry of Li$^+$PF$_6^-$ (top), initial, intermediate, and optimized geometry of Li$^+$PF$_6^-$EC (middle), and optimized Li$^+$PF$_6^-$(EC)$_2$ (bottom) at the LTO surface.

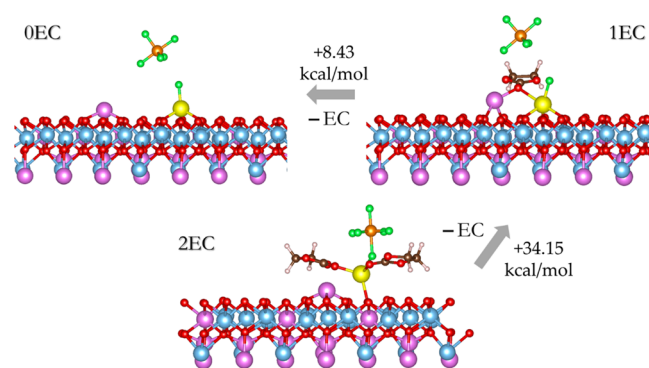**Table 5. Values of AIM Charges (q) and Average Distances from Li$^+$ to the Closest PF$_6^-$ Fluorines, EC Carbonyl (Li$^+$-O$_{EC}$) Oxygens, and Spinel (Li$^+$-O$_{sp}$) Oxygens upon Adsorption at the (111) Face of Li$_4$Ti$_5$O$_{12}$ at Different Degrees of Solvation n. Distances from Li$^+$ to P and from P to the LTO Surface**

| | Li$^+$PF$_6^-$ (EC)$_n$ | | | | | | |
| | distance, Å | | | | | charge | |
n	Li$^+$-P	Li$^+$-F	Li$^+$-O$_{EC}$	Li$^+$-O$_{sp}$	P-O$_{EC}$	P-O$_{surf}$	Li$^+$	PF$_6^-$
0	2.82	1.96		2.24		4.09	0.89	−0.73
1	2.80	1.92	4.80	2.46	4.59	4.37	0.90	−0.83
2	2.83	1.95	1.96	3.68	4.14	4.79	0.89	−0.86

Figure 8. Optimized geometry of Li$^+$Mg^{2+}PF$_6^-$(EC)$_n$, n = 0, 1, and 2 at the (111) LTO surface.

the EC carbonyl oxygen. The next EC molecule fills in the coordination of Mg^{2+}, thus preserving the integrity of the counterion but invoking EC decomposition. This means that in single-cation Mg electrolytes, the noncoordinated Mg^{2+} tears off a F$^-$ from PF$_6^-$, while the well-coordinated Mg^{2+} initiates EC dehydrogenation. The decomposition reactions of EC on the LTO surface mimic the already mentioned phenomenon of LTO gassing in carbonate-based electrolytes. Judging by the amount of released hydrogen in our simulations, it can be inferred that, irrespective of the presence of counterions, the gassing of LTO in EC-based electrolytes is more intense in the presence of Li$^+$ ions than that of Na$^+$ or Mg^{2+}.

The dual-ion complexes display different behavior from the mononuclear ones upon adsorption on LTO. The main difference comes from the robustness of EC even in the presence of PF$_6^-$. This is illustrated on Figure S4 for homonuclear Li$^+$−Li$^+$ and Figure 8 for heteronuclear Li$^+$−Mg^{2+} complexes. In homonuclear complexes, PF$_6^-$ serves as a bridge between the two Li ions sharing the EC, while the introduction of a second EC leads to desorption of the entire complex from the LTO surface as the cations are sharing two solvent molecules and the counterion.

The stronger drive of Mg^{2+} for coordination determines some peculiarities upon the adsorption of heteronuclear dual-cation complexes on LTO surface: The EC molecule becomes nonreactive toward the LTO surface including in the presence of counterion (Figure 8, Table 6, and Figure S4). This signals

that in dual-ion electrolytes, the gassing of LTO will be suppressed in comparison with single-ion electrolytes.

In heteronuclear complexes, the Mg^{2+} ion dictates the manner of coordination of PF$_6^-$ and EC. In the absence of solvent and in the presence of one EC molecule, Mg^{2+} tears off a F$^-$ and a neutral PF$_5$ is released. One solvent molecule keeps the two cations closer than without a counterion (Table 6) although Li$^+$ is at an unfavorable for adsorption position, because after the abstraction of F$^-$, MgF$^+$ is less repulsive than Mg^{2+}. For the same reason, the fully desolvated cations stay closer compared to the case without PF$_6^-$. When two ECs are available, Mg^{2+} coordinates both of them, and attracting a PF$_6^-$ fluorine and the three underlying surface oxygens secures the full coordination number of 6, pushing away Li$^+$. Although a precise quantification of the free energy of desolvation cannot be accomplished due to the multiple processes taking place upon desolvation (anion destruction, ionic bond formation, surface diffusion, adsorption, etc), the total energy change of the stages of solvent removal of the last EC is much smaller in the presence of a counterion, even though the latter is destructed. However, the presence of Mg^{2+} in dual-ion electrolytes stimulates the degradation of the counterion in the last stages of desolvation of dual-ion complexes. This implies that a fluorine-rich solid electrolyte interface will be formed on LTO. This is in agreement with our experimental data on the surface characterization of LTO used as an anode in hybrid metal-ion batteries.[15,26]

Table 6. Values of AIM Charges (q), Average Distances from the Metal Cations to the Closest PF_6^- Fluorines, to the EC Carbonyl (M^{p+}-O_{EC}) and to the Spinel (M^{p+}-O_{sp}) Oxygens upon Adsorption at the (111) Face of $Li_4Ti_5O_{12}$ at Different Degrees of Solvation n. Distances from P to EC and to the LTO Surface of Adsorbed Homonuclear $Li^+(PF_6^-)Li^+(EC)_n$ (see Figure S4) and Heteronuclear $Li^+(PF_6^-)Mg^{2+}(EC)_n$ Dual-Ion Complexes

	$Li^+(PF6^-)Li^+(EC)_n$											
	distances (Å)									charges		
n	$_1Li^+$-$_2Li^+$	$_1Li^+$-O_{EC}	$_2Li^+$-O_{EC}	$_1Li^+$-O_{sp}	$_2Li^+$-O_{sp}	$_1Li^+$-F	$_2Li^+$-F^-	P-O_{EC}	P-O_{surf}	$_1Li^+$	$_2Li^+$	PF_6^-
0	5.83			2.06	2.18	3.65	1.82^a		4.19^a	0.90	0.89	−0.71
1	3.05	2.07	2.06	2.01	2.16	1.94	1.80^a	_3.47_	6.04	0.89	0.92	−0.93^a
2	2.60	1.95	1.94	3.58	3.62	1.89	1.87	_3.69_	6.25	0.90	0.90	−0.93
	$Li^+(PF_6^-)Mg^{2+}(EC)_n$											
	distances (Å)									charges		
n	Li^+-Mg^{2+}	Li^+-O_{EC}	Mg^{2+}-O_{EC}	Li^+-O_{sp}	Mg^{2+}-O_{sp}	Li^+-F	Mg^{2+}-F^-	P-O_{EC}	P-O_{surf}	Li^+	Mg^{2+}	PF_6^-/PF_5^a, F^-
0	5.88			2.03	2.11	4.49	1.82^a		5.34^a	0.99	1.73	−0.02^a, _−0.76_
1	3.53	2.02	2.38	2.01	2.16	3.72	1.84^a	_3.97_	6.04	0.89	1.74	−0.01^a, _−0.72_
2	4.43	4.04	1.99	2.03	2.50	5.83	1.94^b	_3.80_	5.10	0.89	1.76	−0.94^b

^{a}PF_5 instead of PF_6^-. ^{b}$Mg^{2+}PF_6^-$.

CONCLUSIONS

Two groups of conclusions can be outlined from the performed model studies: (i) deductions associated with the choice of model and (ii) interpretation of some experimental results as well as prediction of the LTO behavior toward single- and dual-cation carbonate-based electrolytes.

The model is a compromise between the truthfulness of the physical picture of the process and the computational cost. It comprises several types of interactions: individual interactions of cations and ECs with the surface and interactions among the adsorbates. Moreover, the surface is built of three types of atoms (Li, Ti, and O), and the stoichiometry and the symmetry of the bulk oxide is maintained. All these complexities require the construction of a model in which some implicit and explicit interactions are neglected but the physical essence of the phenomenon is retained. Therefore, we have used a computational scheme for energy calculation, where the surface is sort of a "spectator" in the sense that it appears on both sides of eq 1. Nevertheless, the model is quite reliable as it describes successfully several well-known experimental facts related to the electrochemical properties of LTO as an anode.

In the last stage of desolvation of mononuclear complexes of Li^+, Na^+, or Mg^{2+} in single-cation electrolytes, the interaction of EC with the LTO surface is intensified particularly in the presence of the counterion, leading to solvent degradation and the formation of unwelcome by-products. These reactions are more favorable in Li^+-containing electrolytes than in Na^+- or Mg^{2+}- electrolytes, irrespective of the availability of counterions. This explains the gassing of LTO in Li^+ carbonate-based electrolytes and permits to infer that the gassing will be suppressed in Na^+ and Mg^{2+} electrolytes. This optimistic modeling result is worth experimental confirmation.

Among the three investigated cations, Mg^{2+} is adsorbed most tightly, even when fluorinated, while Li^+ is desorbed most easily. This indicates that Mg^{2+} will form a thicker fluoride-containing film on the LTO surface.

In dual-ion electrolytes, the binuclear complexes are more prone to desolvation in comparison with mononuclear ones. The interaction of EC with the LTO surface is suppressed in dual-ion complexes. However, the slightly solvated binuclear complexes interact preferably with the counterion leading to a release of F^- from PF_6^-.

We trust that the elucidation of the rivalry between LTO-mediated desolvation, degradation, and adsorption can be used as guidelines in understanding of the complex processes occurring at the electrode−electrolyte interface in hybrid-cation batteries emerging as powerful and safe energy storage technologies.

METHODS AND MODELS

Periodic calculations were performed utilizing the projector-augmented wave (PAW) method[47,48] as implemented in the Vienna Ab initio Simulation Package (VASP 5.4.4).[49−51] DFT was employed using the PBE parameterization for the exchange and the correlation energy functionals.[52,53] A plane wave energy cut-off of 450 eV was applied, and the Γ point was used to sample the Brillouin zone. The electron partial occupancies were obtained according to the Gaussian smearing scheme together with a smearing parameter of 0.05 eV. The atomic coordinates of the adsorbed ions and the EC molecules on the surface were optimized toward an energy convergence criteria of 10^{-4} eV between two consecutive geometric steps, and subsequently, the charge distributions were calculated using Bader's quantum theory of atoms in molecules (QTAIM)[54] as implemented in the Bader program.[55] The Gaussian 09 program[56] at the B3LYP/6-31G**/SMD[57−60] level of theory was used for geometry optimization of the isolated cation−organic complexes. VESTA[61] was used for the visualization of optimized periodic structures. Aspects that best visualize the system geometries are selected for the figures.

Simple systems containing a TiO_2 molecule, a metal ion, and an ethylene carbonate molecule were modeled first (Figure S1 and Supporting Information). Free energy calculations (Table S1) reveal that in implicit solvent, most favorable for both Li^+ and Na^+ are: the solvation when the alkali ion is between TiO_2 and EC, and the desolvation when the M^+TiO_2 complex moves away from EC.

For the subsequent model calculations, the (111) oxygen-terminated surface of $Li_4Ti_5O_{12}$ was chosen, as the (111) facet is the most commonly observed one in high-resolution TEM images.[62,63] The experimental study of Kitta et al. concluded that two terminations of the 111-surface are visible: oxygen-

rich and cation-rich.[64] Applying the ab initio thermodynamics approach, the oxygen-rich surface is determined to be the most stable one at potentials above 2 V vs Li$^+$/Li^0 in nanosized LTO.[65,66] Furthermore, the O-terminated (111) surface with stoichiometric Li coverage was theoretically calculated to be the energetically most stable surface of LTO by other authors as well.[67]

It is in these reasons that we chose the (111) face of Li$_4$Ti$_5$O$_{12}$ with a maximum number of oxygens exposed to represent the electrode surface. In order to prepare our model surface, the positions of the atoms from a published crystal structure of Li$_4$Ti$_5$O$_{12}$[68] were optimized in bulk (with a 520 eV energy cut-off), and the relaxed structure was reoriented and cut. The produced slab was repeated three times along the x axis and twice along the y axis (Figure 1). Along the z axis, a ~5 Å thick slab of the spinel was cut, and the cell length was set to 30 Å to ensure that in all of the subsequent calculations, a large enough vacuum layer will be present. On top of the model slab, M$^+$(EC)$_n$, (M$^+$ = Li$^+$, Na$^+$, Mg^{2+}; $n = 0 \div 3$) and M$_1^{p+}$M$_2^{q+}$(EC)$_n$ (M$_1^{p+}$M$_2^{q+}$ = Li$^+$Na$^+$, Li$^+$Mg^{2+}, Na$^+$Mg^{2+}; $n = 0 \div 3$), as well as single-cation- and part of the dual-cation (EC)$_n$ complexes ($n = 0 \div 2$) with PF$_6^-$, were placed at different locations on the (111) face. Only the geometries of the complexes were optimized, assuming a rigid crystal structure of the Li$_4$Ti$_5$O$_{12}$ slab. The most favorable adsorption positions depending on the degree of solvation are determined, and the desolvation and adsorption energies, where possible, were estimated as the energy changes.

$$E_{desolv} = E[\text{slab} + \text{complex(EC)}_{n-1}] + E[\text{EC}]$$
$$- E[\text{slab} + \text{complex(EC)}_n] \quad (1)$$

$$E_{ads}(n) = E^{@\text{slab}}[\text{complex(EC)}_n] - E^{\text{vacuum}}[\text{complex(EC)}_n] \quad (2)$$

Since in eq 1, the energy of the slab appears in two terms with opposite signs, to reduce the computational effort, no dipole and dispersion corrections were applied. The effect of the number of k-points and the thickness of the slab turned out to be systematic and small with respect to the results (Figure S5, Tables S9 and S10, and Supporting Information) but quite substantial in terms of computational load, so we stuck to the minimal yet physically reasonable model.

The bare cations, counterion, and EC molecule were optimized at different positions on the surface. The solvated cationic clusters were preoptimized in earlier studies[27] and placed at selected positions on top of the model surface. A box with the same dimensions was utilized for all periodic calculations ($x/y/z$ = 17.71/20.47/30.0 Å), including single ions or molecules.

ASSOCIATED CONTENT

Ⓢ Supporting Information

The Supporting Information is available free of charge at https://pubs.acs.org/doi/10.1021/acsomega.1c04161.

(Figure S1) Minimalistic models of M$^+$TiO$_2$EC; (Figure S2a) bare EC on LTO surface; (Figure S2b) EC orientation versus the surface; (Figure S3) M$_1^{p+}$M$_2^{q+}$(EC)$_3$ at the (111) LTO surface; (Figure S4) Li$^+$Li$^+$PF$_6^-$(EC)$_n$ at the (111) LTO surface; (Figure S5) model slabs with increased thickness along the z axis; (Table S1) free energy of decomplexation of the minimalistic models; (Table S2) AIM charges of the

different oxygen types on the model surface; (Table S3) adsorption sites with the closest oxygen types; (Table S4) total and relative energy and AIM charges of single ions adsorbed at different sites on the electrode surface; (Table S5) free energy of desolvation in vacuo, in solvent, and on the LTO surface; (Table S6) stabilizing effect of the LTO surface upon desolvation; (Table S7) distances and charges in adsorbed M$_1^{p+}$M$_2^{q+}$(EC)$_3$; (Table S8) distances and charges in adsorbed Na$^+$PF$_6^-$(EC)$_n$ and Mg^{2+}PF$_6^-$ (EC)$_n$; (Table S9) desolvation energy computed with different number of k-points; (Table S10) size effect of the slab along the z axis; ranking of surface adsorption sites; analysis of Table S4; counterion effect on adsorbed M^{p+}(EC)$_n$; sample input file containing the Cartesian coordinates of the surface; effect of k-point number; effect of slab thickness on charges and desolvation energy (PDF)

AUTHOR INFORMATION

Corresponding Authors

Radostina Stoyanova − *Institute of General and Inorganic Chemistry, Bulgarian Academy of Sciences, Sofia 1113, Bulgaria;* ⓘ orcid.org/0000-0002-5815-5131; Email: radstoy@svr.igic.bas.bg

Alia Tadjer − *Faculty of Chemistry and Pharmacy, University of Sofia, Sofia 1164, Bulgaria; Institute of General and Inorganic Chemistry, Bulgarian Academy of Sciences, Sofia 1113, Bulgaria;* ⓘ orcid.org/0000-0002-5405-5037; Email: tadjer@chem.uni-sofia.bg

Author

Hristo Rasheev − *Faculty of Chemistry and Pharmacy, University of Sofia, Sofia 1164, Bulgaria; Institute of General and Inorganic Chemistry, Bulgarian Academy of Sciences, Sofia 1113, Bulgaria*

Complete contact information is available at:
https://pubs.acs.org/10.1021/acsomega.1c04161

Notes
The authors declare no competing financial interest.

■ ACKNOWLEDGMENTS

■ REFERENCES

(1) Dunn, B.; Kamath, H.; Tarascon, J.-M. Electrical Energy Storage for the Grid: A Battery of Choices. *Science* **2011**, *334*, 928−935.

(2) Gür, T.-M. Review of Electrical Energy Storage Technologies, Materials and Systems: Challenges and Prospects for Large-scale Grid Storage. *Energy Environ. Sci.* **2018**, *11*, 2696−2767.

(3) Borah, R.; Hughson, F. R.; Johnston, J.; Nann, T. On Battery Materials and Methods. *Materials Today Advances* **2020**, *6*, 100046.

(4) Yao, H.-R.; You, Y.; Yin, Y.-X.; Wan, L.-J.; Guo, Y.-G. Rechargeable Dual-Metal-Ion Batteries for Advanced Energy Storage. *Phys. Chem. Chem. Phys.* **2016**, *18*, 9326−9333.

(5) Stoyanova, R.; Koleva, V.; Stoyanova, A. Lithium versus Mono/Polyvalent Ion Intercalation: Hybrid Metal Ion Systems for Energy Storage. *Chem. Rec.* **2019**, *19*, 474−501.

(6) Yagi, S.; Ichitsubo, T.; Shirai, Y.; Yanai, S.; Doi, T.; Murase, K.; Matsubara, E. A Concept of Dual-Salt Polyvalent-Metal Storage Battery. *J. Mater. Chem. A* **2014**, *2*, 1144−1149.

(7) Hwang, J.-Y.; Myung, S.-T.; Sun, Y.-K. Sodium-Ion Batteries: Present and Future. *Chem. Soc. Rev.* **2017**, *46*, 3529−3614.

(8) Muldoon, J.; Bucur, C. B.; Gregory, T. Quest for Nonaqueous Multivalent Secondary Batteries: Magnesium and Beyond. *Chem. Rev.* **2014**, *114*, 11683−11720.

(9) de Dompablo, M. E. A.; Ponrouch, A.; Johansson, P.; Palacín, M. R. Achievements, Challenges, and Prospects of Calcium Batteries. *Chem. Rev.* **2020**, *120*, 6331−6357.

(10) Elia, G. A.; Marquardt, K.; Fantini, S.; Lin, R.; Knipping, E.; Peters, W.; Drillet, J. F.; Passerini, S.; Hahn, R.; Hoeppner, K. An Overview and Future Perspectives of Aluminum Batteries. *Adv. Mater.* **2016**, *28*, 7564−7579.

(11) Yi, T.-F.; Yang, S.-Y.; Xie, Y. Recent Advances of $Li_4Ti_5O_{12}$ as a Promising Next Generation Anode Material for High Power Lithium-Ion Batteries. *J. Mater. Chem. A* **2015**, *3*, 5750−5777.

(12) Zhao, B.; Ran, R.; Liu, M.; Shao, Z. A Comprehensive Review of $Li_4Ti_5O_{12}$-Based Electrodes for Lithium-Ion Batteries: The Latest Advancements and Future Perspectives. *Mater. Sci. Eng., R* **2015**, *98*, 1−71.

(13) Sun, Y.; Zhao, L.; Pan, H.; Lu, X.; Gu, L.; Hu, Y.-S.; Li, H.; Armand, M.; Ikuhara, Y.; Chen, L.; Huang, X. Direct Atomic-scale Confirmation of Three-Phase Storage Mechanism in $Li_4Ti_5O_{12}$ Anodes for Room-Temperature Sodium-Ion Batteries. *Nat. Commun.* **2013**, *4*, 1870.

(14) Wu, N.; Yang, Z.-Z.; Yao, H.-R.; Yin, Y.-X.; Gu, L.; Guo, Y.-G. Improving the Electrochemical Performance of the $Li_4Ti_5O_{12}$ Electrode in a Rechargeable Magnesium Battery by Lithium−Magnesium Co-Intercalation. *Angew. Chem., Int. Ed.* **2015**, *54*, 5757−5761.

(15) Ivanova, S.; Zhecheva, E.; Kukeva, R.; Nihtianova, D.; Mihaylov, L.; Atanasova, G.; Stoyanova, R. Layered P3-$Na_xCo_{1/3}Ni_{1/3}Mn_{1/3}O_2$ versus Spinel $Li_4Ti_5O_{12}$ as a Positive and a Negative Electrode in a Full Sodium−Lithium Cell. *ACS Appl. Mater. Interfaces* **2016**, *8*, 17321−17333.

(16) Ohzuku, T.; Ueda, A.; Yamamoto, N. Zero-Strain Insertion Material of $Li[Li_{1/3}Ti_{5/3}]O_4$ for Rechargeable Lithium Cells. *J. Electrochem. Soc.* **1995**, *142*, 1431−1435.

(17) Ma, Z.; MacFarlane, D.; Kar, M. Mg Cathode Materials and Electrolytes for Rechargeable Mg Batteries: A Review. *Batteries Supercaps* **2019**, *2*, 115−127.

(18) Cheng, Y.; Chang, H. J.; Dong, H.; Choi, D.; Sprenkle, V. L.; Liu, J.; Yao, Y.; Li, G. Rechargeable Mg−Li Hybrid Batteries: Status and Challenges. *J. Mater. Res.* **2016**, *31*, 3125−3141.

(19) Dong, H.; Li, Y.; Liang, Y.; Li, G.; Sun, C.-J.; Ren, Y.; Lu, Y.; Yao, Y. A Magnesium−Sodium Hybrid Battery with High Operating Voltage. *Chem. Commun.* **2016**, *52*, 8263−8266.

(20) Song, J.; Sahadeo, E.; Noked, M.; Lee, S. B. Mapping the Challenges of Magnesium Battery. *J. Phys. Chem. Lett.* **2016**, *7*, 1736−1749.

(21) Son, S.-B.; Gao, T.; Harvey, S. P.; Steirer, K.; Stokes, A.; Norman, A.; Wang, C.; Cresce, A.; Xu, K.; Ban, C. An Artificial Interphase Enables Reversible Magnesium Chemistry in Carbonate Electrolytes. *Nat. Chem.* **2018**, *10*, 532−539.

(22) Jónsson, E.; Johansson, P. Modern Battery Electrolytes: Ion−Ion Interactions in Li^+/Na^+ Conductors from DFT Calculations. *Phys. Chem. Chem. Phys.* **2012**, *14*, 10774−10779.

(23) Kimura, T.; Fujii, K.; Sato, Y.; Morita, M.; Yoshimoto, N. Solvation of Magnesium Ion in Triglyme-Based Electrolyte Solutions. *J. Phys. Chem. C* **2015**, *119*, 18911−18917.

(24) Pham, T. A.; Kweon, K. E.; Samanta, A.; Lordi, V.; Pask, J. E. *J. Phys. Chem. C* **2017**, *121*, 21913−21920.

(25) Samuel, D.; Steinhauser, C.; Smith, J. G.; Kaufman, A.; Radin, M. D.; Naruse, J.; Hiramatsu, H.; Siegel, D. J. Ion Pairing and Diffusion in Magnesium Electrolytes Based on Magnesium Borohydride. *ACS Appl. Mater. Interfaces* **2017**, *9*, 43755−43766.

(26) Kalapsazova, M.; Rasheev, H.; Zhecheva, E.; Tadjer, A.; Stoyanova, R. Insights into the Function of Electrode and Electrolyte Materials in a Hybrid Lithium−Sodium Ion Cell. *J. Phys. Chem. C* **2019**, *123*, 11508−11521.

(27) Rasheev, H.; Stoyanova, R.; Tadjer, A. Dual-Metal Electrolytes for Hybrid-Ion Batteries: Synergism or Antagonism? *ChemPhysChem* **2021**, *22*, 1110−1123.

(28) Jow, T. R.; Delp, S. A.; Allen, J. L.; Jones, J.-P.; Smart, M. C. Factors Limiting Li^+ Charge Transfer Kinetics in Li-Ion Batteries. *J. Electrochem. Soc.* **2018**, *165*, A361.

(29) Jorn, R.; Raguette, L.; Peart, S. Investigating the Mechanism of Lithium Transport at Solid Electrolyte Interphases. *J. Phys. Chem. C* **2020**, *124*, 16261−16270.

(30) Yua, X.; Manthiram, A. Electrode−Electrolyte Interfaces in Lithium-Based Batteries. *Energy Environ. Sci.* **2018**, *11*, 527−543.

(31) Li, Q.; Lu, D.; Zheng, J.; Jiao, S.; Luo, L.; Wang, C.-M.; Xu, K.; Zhang, J.-G.; Xu, W. Li^+-Desolvation Dictating Lithium-Ion Battery's Low-Temperature Performances. *ACS Appl. Mater. Interfaces* **2017**, *9*, 42761−42768.

(32) Okoshi, M.; Yamada, Y.; Yamada, A.; Nakai, H. Theoretical Analysis on De-Solvation of Lithium, Sodium, and Magnesium Cations to Organic Electrolyte Solvents. *J. Electrochem. Soc.* **2013**, *160*, A2160−A2165.

(33) Åvall, G.; Mindemark, J.; Brandell, D.; Johansson, P. Sodium-Ion Battery Electrolytes: Modeling and Simulations. *Adv. Energy Mater.* **2018**, *8*, 1703036.

(34) von Wald Cresce, A.; Gobet, M.; Borodin, O.; Peng, J.; Russell, S. M.; Wikner, E.; Fu, A.; Hu, L.; Lee, H.-S.; Zhang, Z.; Yang, X.-Q.; Greenbaum, S.; Amine, K.; Xu, K. Anion Solvation in Carbonate-Based Electrolytes. *J. Phys. Chem. C* **2015**, *119*, 27255−27264.

(35) Tominaga, Y.; Yamazaki, K.; Nanthana, V. Effect of Anions on Lithium Ion Conduction in Poly(ethylene carbonate)-Based Polymer Electrolytes. *J. Electrochem. Soc.* **2015**, *162*, A3133.

(36) Xu, K.; von Wald Cresce, A. Li^+-Solvation/Desolvation Dictates Interphasial Processes on Graphitic Anode in Li Ion Cells. *J. Mater. Res.* **2012**, *27*, 2327.

(37) Yao, Y.-X.; Yan, C.; Zhang, Q. Emerging Interfacial Chemistry of Graphite Anodes in Lithium-Ion Batteries. *Chem. Commun.* **2020**, *56*, 14570−14584.

(38) Leanza, D.; Vaz, C. A. F.; Czekaj, I.; Novák, P.; El Kazzi, M. Solving the Puzzle of $Li_4Ti_5O_{12}$ Surface Reactivity in Aprotic Electrolytes in Li-Ion Batteries by Nanoscale XPEEM Spectromicroscopy. *J. Mater. Chem. A* **2018**, *6*, 3534.

(39) Xu, K.; von Wald Cresce, A.; Lee, U. Differentiating Contributions to "Ion Transfer" Barrier from Interphasial Resistance and Li^+ Desolvation at Electrolyte/Graphite Interface. *Langmuir* **2010**, *26*, 11538−11543.

(40) Haruyama, J.; Ikeshoji, T.; Otani, M. Analysis of Lithium Insertion/Desorption Reaction at Interfaces between Graphite Electrodes and Electrolyte Solution Using Density Functional + Implicit Solvation Theory. *J. Phys. Chem. C* **2018**, *122*, 9804−9810.

(41) Pham, T. A.; Kweon, K. E.; Samanta, A.; Ong, M. T.; Lordi, V.; Pask, J. E. Intercalation of Lithium into Graphite: Insights from First-Principles Simulations. *J. Phys. Chem. C* **2020**, *124*, 21985−21992.

(42) He, Y.-B.; Li, B.; Liu, M.; Zhang, C.; Lv, W.; Yang, C.; Li, J.; Du, H.; Zhang, B.; Yang, Q.-H.; Kim, J.-K.; Kang, F. Gassing in $Li_4Ti_5O_{12}$-based batteries and its remedy. *Sci. Rep.* **2012**, *2*, 913.

(43) Wu, K.; Yang, J.; Zhang, Y.; Wang, C.; Wang, D. Investigation on $Li_4Ti_5O_{12}$ Batteries Developed for Hybrid Electric Vehicle. *J. Appl. Electrochem.* **2012**, *42*, 989−995.

(44) Wu, K.; Yang, J.; Liu, Y.; Zhang, Y.; Wang, C.; Xu, J.; Ning, F.; Wang, D. Investigation on Gas Generation of $Li_4Ti_5O_{12}$/$LiNi_{1/3}Co_{1/3}Mn_{1/3}O_2$ Cells at Elevated Temperature. *J. Power Sources* **2013**, *237*, 285−290.

(45) Wang, Y.; Zhao, J.; Qu, J.; Wei, F.; Song, W.; Guo, Y.-G.; Xu, B. Investigation into the Surface Chemistry of $Li_4Ti_5O_{12}$ Nanoparticles

for Lithium Ion Batteries. *ACS Appl. Mater. Interfaces* **2016**, *8*, 26008−26012.

(46) Guo, J.; Zuo, W.; Cai, Y.; Chen, S.; Zhang, S.; Liu, J. A Novel $Li_4Ti_5O_{12}$-Based High-Performance Lithium-Ion Electrode at Elevated Temperature. *J. Mater. Chem. A* **2015**, *3*, 4938−4944.

(47) Blöchl, P. E. Projector augmented-wave method. *Phys. Rev. B* **1994**, *50*, 17953.

(48) Kresse, G.; Joubert, D. From Ultrasoft Pseudopotentials to the Projector Augmented-Wave Method. *Phys. Rev. B* **1999**, *59*, 1758.

(49) Kresse, G.; Hafner, J. *Ab Initio* Molecular Dynamics for Liquid Metals. *Phys. Rev. B: Condens. Matter Mater. Phys.* **1993**, *47*, 558.

(50) Kresse, G.; Furthmüller, J. Efficient Iterative Schemes for *Ab Initio* Total-Energy Calculations Using a Plane-Wave Basis Set. *Phys. Rev. B: Condens. Matter Mater. Phys.* **1996**, *54*, 11169.

(51) Kresse, G.; Furthmüller, J. Efficiency of Ab-initio Total Energy Calculations for Metals and Semiconductors Using a Plane-Wave Basis Set. *Comput. Mater. Sci.* **1996**, *6*, 15−50.

(52) Perdew, J. P.; Burke, K.; Ernzerhof, M. Generalized Gradient Approximation Made Simple. *Phys. Rev. Lett.* **1996**, *77*, 3865.

(53) Perdew, J. P.; Burke, K.; Ernzerhof, M. Erratum: Generalized Gradient Approximation Made Simple. *Phys. Rev. Lett.* **1997**, *78*, 1396.

(54) Bader, R. F. W. Atoms in Molecules. *Acc. Chem. Res.* **1985**, *18*, 9−15.

(55) Tang, W.; Sanville, E.; Henkelman, G. A Grid-Based Bader Analysis Algorithm Without Lattice Bias. *J. Phys.: Condens. Matter* **2009**, *21*, No. 084204.

(56) Frisch, M. J.; Trucks, G. W.; Schlegel, H. B.; Scuseria, G. E.; Robb, M. A.; Cheeseman, J. R.; Scalmani, G.; Barone, V.; Mennucci, B.; Petersson, G. A.; Nakatsuji, H.; Caricato, M.; Li, X.; Hratchian, H. P.; Izmaylov, A. F.; Bloino, J.; Zheng, G.; Staroverov, V. N.; Kobayashi, R.; Normand, J.; Raghavachari, K.; Rendell, A.; Burant, J. C.; Iyengar, S. S.; Tomasi, J.; Cossi, M.; Rega, N.; Millam, N. J.; Klene, M.; Knox, J. E.; Cross, J. B.; Bakken, V.; Adamo, C.; Jaramillo, J.; Gomperts, R.; Stratmann, R. E.; Yazyev, O.; Austin, A. J.; Cammi, R.; Pomelli, C.; Ochterski, J. W.; Martin, R. L.; Morokuma, K.; Zakrzewski, V. G.; Voth, G. A.; Salvador, P.; Dannenberg, J. J.; Dapprich, S.; Daniels, A. D.; Farkas, Ö.; Foresman, J. B.; Ortiz, J. V.; Cioslowski, J.; Fox, D. J., *Gaussian 09, Revision D.01*; Gaussian, Inc.: Wallingford CT, 2013.

(57) Becke, A. D. Density-Functional Thermochemistry. III. The Role of Exact Exchange. *J. Chem. Phys.* **1993**, *98*, 5648−5652.

(58) Lee, C.; Yang, W.; Parr, R. G. Development of the Colle-Salvetti Correlation-Energy Formula into a Functional of the Electron Density. *Phys. Rev. B* **1988**, *37*, 785−789.

(59) Francl, M. M.; Pietro, W. J.; Hehre, W. J.; Binkley, J. S.; DeFrees, D. J.; Pople, J. A.; Gordon, M. S. Self-Consistent Molecular Orbital Methods. XXIII. A Polarization-Type Basis Set for Second-Row Elements. *J. Chem. Phys.* **1982**, *77*, 3654.

(60) Marenich, A.; Cramer, C. J.; Truhlar, D. G. Universal Solvation Model Based on Solute Electron Density and on a Continuum Model of the Solvent Defined by the Bulk Dielectric Constant and Atomic Surface Tensions. *J. Phys. Chem. B.* **2009**, *113*, 6378−6396.

(61) Momma, K.; Izumi, F. VESTA 3 for three-dimensional visualization of crystal, volumetric and morphology data. *J. Appl. Crystallogr.* **2011**, *44*, 1272−1276.

(62) Gao, Y.; Wang, Z.; Chen, L. Stability of Spinel $Li_4Ti_5O_{12}$ in Air. *J. Power Sources* **2014**, *245*, 684−690.

(63) Cunha, D. M.; Hendriks, T. A.; Vasileiadis, A.; Vos, C. M.; Verhallen, T.; Singh, D. P.; Wagemaker, M.; Huijben, M. Doubling Reversible Capacities in Epitaxial $Li_4Ti_5O_{12}$ Thin Film Anodes for Microbatteries. *ACS Appl. Energy Mater.* **2019**, *2*, 3410−3418.

(64) Kitta, M.; Matsuda, T.; Maeda, Y.; Akita, T.; Tanaka, S.; Kido, Y.; Kohyama, M. Atomistic Structure of a Spinel $Li_4Ti_5O_{12}$ (111) Surface Elucidated by Scanning Tunneling Microscopy and Medium Energy Ion Scattering Spectrometry. *Surf. Sci.* **2014**, *619*, 5−9.

(65) Exner, K. S. Constrained Ab Initio Thermodynamics: Transferring the Concept of Surface Pourbaix Diagrams in Electro-catalysis to Electrode Materials in Lithium-Ion Batteries. *ChemElectroChem* **2017**, *4*, 3231−3237.

(66) Exner, K. S. Activity − Stability Volcano Plots for the Investigation of Nano-Sized Electrode Materials in Lithium-Ion Batteries. *ChemElectroChem* **2018**, *5*, 3243−3248.

(67) Morgan, B. J.; Carrasco, J.; Teobaldi, G. Variation in Surface Energy and Reduction Drive of a Metal Oxide Lithium-Ion Anode with Stoichiometry: A DFT Study of Lithium Titanate Spinel Surfaces. *J. Mater. Chem. A* **2016**, *4*, 17180−17192.

(68) Deschanvres, A.; Raveau, B.; Sekkal, Z. Mise en Evidence et Etude Cristallographique d'une Nouvelle Solution Solide de Type Spinelle $Li_{1+x}Ti_{2−x}O_4$ $0 \leqslant x \leqslant 0, 33_3$. *Mater. Res. Bull.* **1971**, *6*, 699−704.